

Link Budget Modeling for Q-Band LEO Satellite Communications with Adaptive Coding and Modulation

Ioannis Ziargas ^{ID}, *University of the Peloponnese*⁽¹⁾

Supervisor: Panagiotis Zervas ^{ID}, *University of the Peloponnese*⁽²⁾

Abstract—We present a modeling and evaluation framework for *Q*-band LEO satellite links that integrates time-varying propagation, realistic noise temperature modeling and adaptive coding and modulation (ACM). Satellite passes are simulated at 1 Hz and paired with co-located meteorological measurements resampled from 10-minute data to 1-second resolution. Atmospheric absorption, clouds and rain are combined into an excess path loss (EPL) term, which feeds the computation of sky brightness and system noise temperature for uplink and downlink. The link budget then produces C/N_0 time series that drive an ACM selector based on Shannon-consistent E_b/N_0 thresholds with implementation margin and hysteresis. We report contrasting case studies: a stable pass where both directions hold the highest-rate MODCOD continuously (≈ 947 Mbit/s) and a degraded pass with deep fades that force frequent mode changes and sustained throughput reductions. The results show that (i) sidelobe coupling to atmospheric emission materially raises downlink noise temperature, (ii) uplink spillover toward cold space lowers the satellite receiver's effective temperature, and (iii) modest hysteresis prevents oscillations without sacrificing throughput. The framework supports parameter sweeps and can incorporate measured hardware figures to align with operational systems, providing a practical basis for dynamic link assessment and handover policy design.

Index Terms—Satellite communication, LEO Satellites, Link budgets, Adaptive modulation and coding (AMC/ACM), radio propagation, mmWave propagation, sky brightness temperature, system noise temperature, spectral efficiency, Shannon capacity, time-varying channels, hysteresis-based ACM, uplink/downlink analysis, meteorological data resampling.

I. INTRODUCTION

SATELLITE communication (SATCOM) systems are a key enabler of global connectivity, supporting services such as broadband internet, telecommunications, Earth observation, and navigation [1], [2]. At the core of SATCOM design and optimization is the link budget, which accounts for all gains and losses a signal experiences as it propagates between a transmitter and a receiver [2], [3]. The link budget not only determines whether a communication link can meet quality-of-service (QoS) requirements but also guides the selection of

⁽¹⁾The author is with the School of Electrical and Computer Engineering, University of the Peloponnese, Patras, Greece (e-mail: ece20229@go.uop.gr). This paper was submitted as the semester project for the course **Information Theory (ECE_TEL851)** during the 2025 spring semester.

⁽²⁾The supervisor, Associate Professor at the School of Electrical and Computer Engineering, University of the Peloponnese, Greece (email: pzervas@go.uop.gr), is serving as the instructor for the course **Information Theory (ECE_TEL851)** during the 2025 spring semester.

antenna sizes, transmission power levels, and system margins [2], [3].

The rapid deployment of large-scale low Earth orbit (LEO) satellite constellations has created both new opportunities and challenges for link budget analysis. Unlike geostationary (GEO) satellites, which remain fixed relative to the Earth's surface, LEO satellites operate at lower altitudes and move quickly across the sky. This motion leads to frequent handovers between satellites, time-varying propagation distances, and changing elevation angles. As a result, free-space path loss, atmospheric absorption, and weather-related attenuation all vary dynamically. These effects are particularly noticeable in higher-frequency bands, such as K_u and K_a , with growing interest in the *Q* and *V* bands, where rain, cloud and gaseous attenuation can significantly degrade link performance [4]–[7].

Traditional link budget calculations often assume static conditions or rely on simplified atmospheric models, which may underestimate the impact of environmental effects. These limitations are further magnified by the increasing severity and frequency of extreme weather events associated with climate change [8]. To support next-generation satellite systems, more accurate and adaptive approaches are needed. Incorporating realistic atmospheric attenuation models which are validated through measurements or predictive algorithms into link budget frameworks, enables more reliable performance evaluations and more informed network design decisions.

A. RELATED WORK

In our earlier study [9], we developed a framework to simulate the trajectories of five LEO satellites on March 29, 2025. This date was selected to align with the availability of measured weather data from a ground-based station located approximately 1.77 km from the simulated ground station. The weather station, positioned at 38.23444° N and 21.74333° E at a similar altitude to the simulated ground station (38.21868° N, 21.74641° E), is operated by Mr. Giorgos Chronopoulos in collaboration with the National Observatory of Athens [10], [11]. The satellite trajectories were generated with a 1-second resolution using the Keplerian elements listed in Appendix C, providing detailed position data for the entire day. A ground station model was also included to establish links with the satellites, resulting in a total of 19 visible passes. For simplicity, the antennas of both the ground station and satellites were not explicitly modeled, and the effective isotropic radiated

power (EIRP) was assumed to remain constant at maximum gain throughout each pass.

To match the trajectory resolution, the measured rain rate which was originally provided at 10-minute intervals, was interpolated to 1-second intervals using a Gamma auto-regressive distribution. Based on this dataset, atmospheric absorption was calculated and rain-induced attenuation was modeled as a Gaussian random process, which also statistically account for cloud attenuation. These components were combined to obtain the total excess path loss (EPL) as a function of elevation angle and frequency. The resulting EPL data from 18 satellite passes were then used to train a Long Short-Term Memory (LSTM) neural network, with the 19th pass reserved for testing. The model demonstrated high accuracy in predicting EPL.

B. CONTRIBUTIONS AND PAPER SCOPE

Building on this foundation and using the same satellite passes together with the measured weather data, the present work extends the analysis by incorporating the calculated EPL into a complete link budget evaluation. This approach enables performance assessment under realistic, time-varying propagation conditions, considering both uplink and downlink. The analysis further supports dynamic evaluation of system parameters and the application of adaptive modulation and coding schemes to maintain reliable performance under varying channel conditions.

The remainder of this paper is organized as follows. Sec. II introduces the fundamental principles of link budget analysis. Sec. III describes the interpolation of measured weather data to match the resolution of the satellite orbital trajectories and EPL calculations. Sec. IV presents the modeling of the total system noise, including contributions from internal electronics, antennas, and the propagation channel. Sec. V outlines the implementation of adaptive coding and modulation based on channel characteristics, and Sec. VI presents the resulting ACM performance for two satellite passes.

II. LINK BUDGET FUNDAMENTALS

Link budget analysis is a fundamental tool in wireless communications. It provides a detailed accounting of all gains and losses that a signal experiences as it propagates from the transmitter, through space and the atmosphere, to the receiver. It defines the key parameters required for system design, including the configuration of electronic components, as well as the coding rates and modulation schemes necessary to meet performance targets [1], [2]. It also provides an estimate of the received carrier power, which is essential for verifying the feasibility and reliability of the communication system. Beyond received power, the link budget forms the basis for calculating the carrier-to-noise ratio (C/N_o), signal-to-noise ratio (SNR) and bit error rate (BER), which are critical performance metrics. Fig. 1 shows the block diagram of the link budget analysis, highlighting the parameters considered in the process. The general mathematical form of the received carrier power is given by:

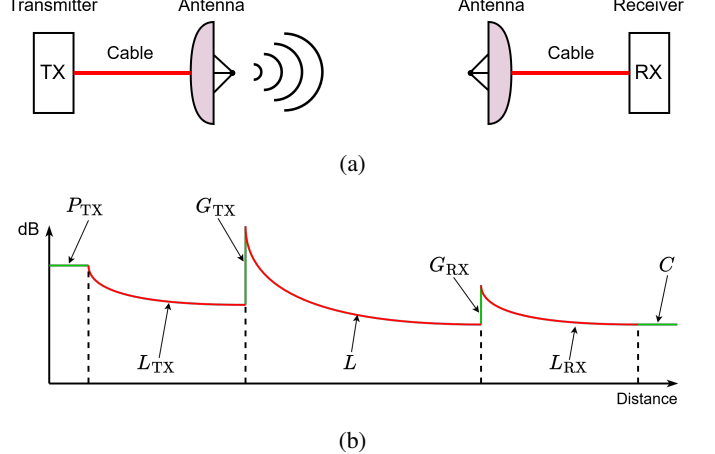


Fig. 1: Communication link representation. (a) Block diagram of a radio link, showing the transmitter, feeder cable, transmitting antenna, free-space propagation, receiving antenna, and receiver cable leading to the receiver. (b) Corresponding link power budget in logarithmic scale, where the transmitted power P_{TX} is reduced by the transmitter feeder loss L_{TX} , increased by the transmitting antenna gain G_{TX} , attenuated by the total channel losses L , increased by the receiving antenna gain G_{RX} and reduced by the receiver feeder loss L_{RX} , resulting in the received carrier power C

$$C = \underbrace{P_{\text{TX}} - L_{\text{TX}} + G_{\text{TX}}}_{\text{EIRP}} - L + G_{\text{RX}} - L_{\text{RX}} \quad (\text{dBW}) \quad (1)$$

In this expression, P_{TX} is the transmit power in dBW, L_{TX} is the transmit feeder loss in dB, G_{TX} is the transmit antenna gain in dBi, L is the total radio channel loss in dB, G_{RX} is the receive antenna gain in dBi and L_{RX} is the receiver feeder loss in dB [2], [3]. The link budget consists of two main components: the uplink, which refers to signal transmission from the ground station to the satellite, and the downlink, which refers to transmission from the satellite to the ground station. Each path is influenced by different transmission powers, antenna gains, and atmospheric conditions. In this study, the antenna and hardware parameters ($P_{\text{TX}}, L_{\text{TX}}, G_{\text{TX}}, G_{\text{RX}}, L_{\text{RX}}$) are assumed values because detailed antenna and RF hardware modeling has not been performed. The total radio channel loss is defined as the combination of free-space path loss (FSPL) and excess path loss (EPL) caused by atmospheric absorption, rain and cloud attenuation [4]–[7]:

$$L = l_{\text{FSPL}} + l_{\text{EPL}} \quad (\text{dB}) \quad (2)$$

where l_{EPL} is the EPL, as calculated in (cite the previous work) and l_{FSPL} is the FSPL expressed as a function of the elevation angle θ :

$$l_{\text{FSPL}}(\theta) = 20\log_{10}(d(\theta)) + 20\log_{10}(f_c) - 147.55 \quad (\text{dB}) \quad (3)$$

where d is the slant range in meters between the satellite and the ground station, calculated in MATLAB using the Satellite

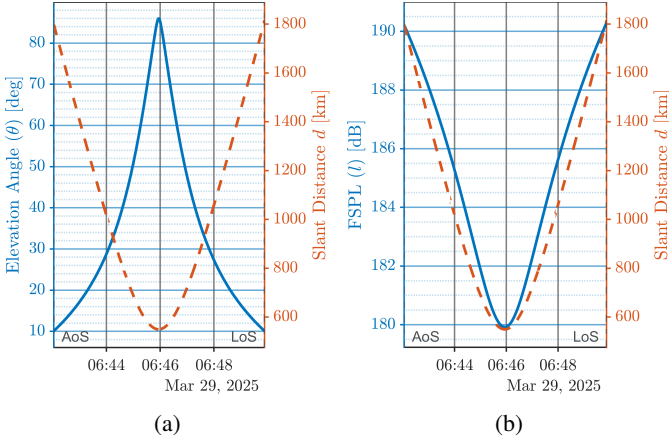


Fig. 2: Satellite pass geometry and free-space path loss for the first pass of satellite 5 on March 29, 2025, occurring between 06:42:03 and 06:49:53 (7 min, 50 s). The results were generated using the Keplerian elements provided in Appendix C. (a) Elevation angle θ and corresponding slant distance d during the pass. (b) FSPL and slant distance d for the same pass.

Communications and Aerospace Toolboxes as a function of the elevation angle θ . As the elevation angle increases toward zenith, the slant range decreases, resulting in lower FSPL, as shown in Fig. 2. This effect is important because FSPL typically represents the dominant source of attenuation under clear-sky conditions. The parameter f_c is the carrier frequency in Hz, which must comply with spectrum allocations defined by the International Telecommunication Union (ITU) in the Radio Regulations, Article 5 [12]. For this study, since the simulation is based in Greece, the frequency allocations follow the regulations of the Hellenic Telecommunications and Post Commission (EETT) [13]. Accordingly, we assume operating at 43 GHz for the uplink and 42 GHz for the downlink [14].

III. METEOROLOGICAL DATA PROCESSING AND INTERPOLATION

The meteorological parameters—surface temperature (T_s), surface pressure (P_s) and dew point (T_d)—were recorded by the Patras Prosygika weather station [10] at 10-minute intervals. To match the satellite trajectory resolution of 1 Hz, the data were linearly interpolated to 1-second spacing within each interval $[t_i, t_{i+1}]$. This method was selected because the parameters vary gradually and linear interpolation provides sufficient accuracy with low computational cost, as seen in Fig. 3. Let $X \in \{T_s, P_s, T_d\}$ denote a generic parameter with values X_i and X_{i+1} at times t_i and t_{i+1} , respectively. The uniformly spaced time grid is defined as:

$$t_k = t_i + k\Delta_t, \quad k = 0, 1, \dots, n - 1$$

where Δ_t is the target sampling interval ($\Delta_t = 1$ s) and

$$n = \left\lfloor \frac{t_{i+1} - t_i}{\Delta_t} \right\rfloor$$

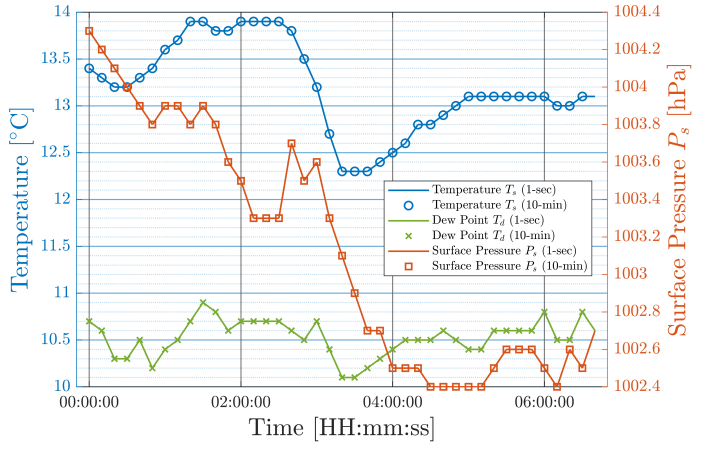


Fig. 3: Surface meteorological parameters. Surface temperature T_s , dew point temperature T_d and surface pressure P_s with 10-minute measurements and 1-second interpolated data. Temperature and dew point are shown on the left axis in $^{\circ}\text{C}$ and surface pressure on the right axis in hPa.

Here, n represents the total number of interpolated samples in the interval $[t_i, t_{i+1}]$, corresponding to the duration of the interval expressed in integer multiples of Δ_t . The interpolated values at each time instant t_k are then computed as:

$$X(t_k) = X_i + \frac{X_{i+1} - X_i}{t_{i+1} - t_i} (t_k - t_i), \quad k = 0, \dots, n - 1 \quad (4)$$

This approach ensures a smooth progression of each parameter between consecutive measurements, while excluding the right endpoint t_{i+1} to avoid duplicate samples across adjacent intervals. Physical constraints are also applied to maintain realistic values, with the dew point restricted not to exceed the air temperature. The resulting interpolation can be seen in Fig. 3. From these interpolated variables, the water vapor density ρ_{ws} , can be derived, since it cannot be measured directly with standard weather station equipment. Using the Magnus–Tetens approximation, the actual vapor pressure at the dew point is first obtained as

$$e(T_d) = 6.112 \exp \left(\frac{17.62 T_d}{243.12 + T_d} \right) \text{ (hPa)} \quad (5)$$

where T_d is the dew point temperature in degrees Celsius [15]. The constants 6.112, 17.62, and 243.12 are fitted parameters that make the formula accurate for typical meteorological conditions in the range of approximately -45°C to $+60^{\circ}\text{C}$. The water vapor density is then expressed as

$$\rho_{ws} = \frac{216.7 e}{T_s} \text{ (g/m}^3\text{)} \quad (6)$$

where T_s is the surface air temperature in Kelvin and e is the vapor pressure in hPa [16]. The constant 216.7 results from $\frac{1000}{R_v}$ after unit conversions, $R_v \approx 461.5 \text{ (J}\cdot\text{kg}^{-1}\cdot\text{K}^{-1}$) being the specific gas constant for water vapor [16]. Once ρ_{ws} is calculated, along with the interpolated surface temperature and pressure, these parameters serve as inputs to the calculation of the mean radiating temperature of the atmosphere further discussed in Sec. IV-B.

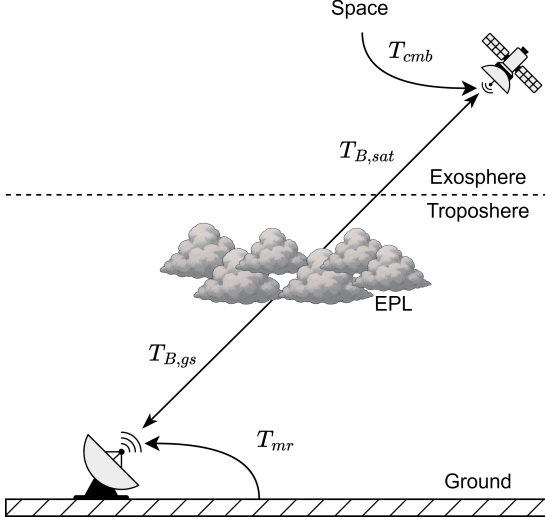


Fig. 4: Noise temperature contributions in a satellite communication link. From space, the cosmic microwave background contributes T_{cmb} , while the satellite itself introduces an equivalent body noise temperature $T_{B,sat}$. As the signal propagates through the atmosphere, it undergoes excess path loss (EPL) primarily in the troposphere. At the ground station, the receiving antenna collects additional thermal radiation represented by $T_{B,gs}$, while the atmosphere introduces an effective noise contribution T_{mr} .

IV. SYSTEM NOISE TEMPERATURE MODEL

As shown in Eq. 1, the link budget quantifies the received carrier power after all transmission gains and channel losses are applied. This parameter is essential for evaluating system feasibility. However, received carrier power alone does not fully determine link performance. To accurately assess the quality of a communication link, it must be considered alongside the noise introduced during propagation and within the receiver. Thermal noise is often represented using the Additive White Gaussian Noise (AWGN) model. While this statistical model is useful for simple analysis, it does not capture the physical origins of noise. In practice, thermal noise arises from two main sources: external noise from the environment, illustrated in Fig. 4 in which the ground station operates and internal noise generated by the electronic components of the transmitting and receiving systems, illustrated in Fig. 5. These contributions are combined into the system noise temperature, which defines the effective noise level experienced by the system and is expressed as:

$$N_0 = kT_{sys} \quad (\text{W/Hz}) \quad (7)$$

where k is Boltzmann's constant and T_{sys} is the effective system noise temperature [3]. The latter is composed of the atmospheric noise temperature and the internal noise of the receiver, given by:

$$T_{sys} = T_{in} + T_{eRX} \quad (\text{K}) \quad (8)$$

The parameter T_{in} is defined in Sec. IV-E, while T_{eRX} is described in Sec. IV-A. Accurate modeling of T_{sys} is critical

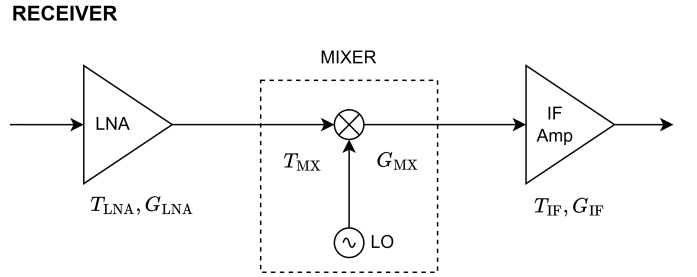


Fig. 5: Receiver block diagram with low-noise amplifier (LNA), mixer driven by the local oscillator (LO) and intermediate-frequency (IF) amplifier, characterized by their respective noise temperatures and gains.

because it directly affects the noise level against which the received carrier power must be evaluated. This ensures that the calculated link parameters reflect realistic operating conditions and that the communication link can achieve the desired quality of service.

A. RECEIVER INTERNAL NOISE

The internal noise temperature T_{eRX} characterizes the noise generated by the electronic components of the receiver chain, as illustrated in Fig. 5. Each device, such as the low-noise amplifier (LNA), mixer and intermediate frequency (IF) amplifier, contributes thermal noise that can be modeled as an equivalent input noise source. The equivalent noise temperature of a device is related to its noise figure F by:

$$T_e = T_0(F - 1) \quad (\text{K}) \quad (9)$$

where $T_0 = 290$ K is the standard reference temperature [2]. For cascaded devices, the overall receiver noise temperature is not a simple sum of individual contributions, since the gain of each stage reduces the relative impact of subsequent stages. Instead, the Friis equation in noise temperature form is applied:

$$T_{eRX} = T_{LNA} + \frac{T_{MX}}{G_{LNA,\text{lin}}} + \frac{T_{IF}}{G_{LNA,\text{lin}}G_{MX,\text{lin}}} \quad (\text{K}) \quad (10)$$

Here, T_{LNA} is the noise temperature of the LNA in Kelvin K, T_{MX} is the noise temperature of the mixer in K and T_{IF} is the noise temperature of the IF amplifier in K. The terms $G_{LNA,\text{lin}}$ and $G_{MX,\text{lin}}$ denote the LNA gain and mixer gain, respectively, expressed in linear scale [2], [17]. This relationship highlights the critical role of the LNA. A low-noise, high-gain front-end amplifier ensures that the noise contribution of later stages is significantly suppressed. For example, while mixers may exhibit noise temperatures on the order of hundreds of kelvins, their effective contribution is reduced to only a few kelvins when preceded by an LNA with sufficient gain. As a result, the receiver noise temperature is typically dominated by the first stage. Optimizing this stage is essential to achieving the low overall system noise temperature required for high-frequency satellite communication links.

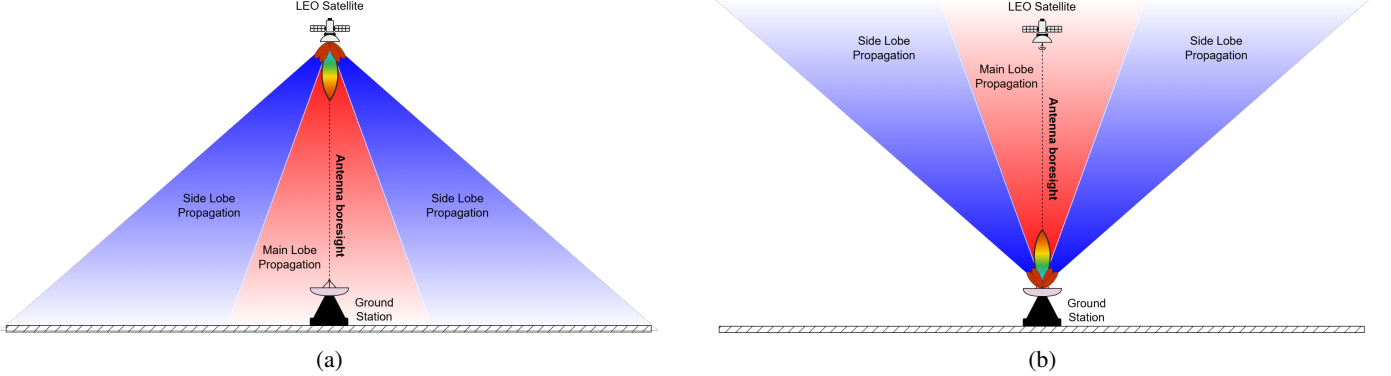


Fig. 6: Antenna radiation patterns for satellite downlink and uplink. In the downlink case (a), the satellite antenna directs its main lobe along the boresight toward the ground station, providing maximum signal strength within the coverage area. Side lobes radiate energy at lower levels outside the main beam, where they interact with the Earth's atmosphere and contribute additional noise to the system. In the uplink case (b), the ground station antenna forms a main lobe aligned with the boresight toward the satellite. Here, the side lobe spillover is directed toward space, where it couples primarily with the cosmic background noise, which is significantly lower than the atmospheric noise encountered in the downlink.

B. ATMOSPHERIC NOISE TEMPERATURE

The atmospheric noise temperature (T_A) represents the effective thermal radiation emitted by the Earth's atmosphere due to absorption and re-emission by atmospheric gases, clouds, and hydrometeors. When a radio signal propagates through the atmosphere, molecules such as oxygen and water vapor absorb part of the energy and then re-radiate it as noise toward the receiving antenna. This process is quantified as an equivalent noise temperature that adds directly to the system noise, as illustrated in Fig. 4. In practice, the atmospheric noise temperature is expressed as the sky brightness temperature, which depends on frequency, elevation angle, and local meteorological conditions. ITU-R P.372-17 [18] provides the following mathematical model which expresses the sky brightness temperature:

$$T_B = 2.73 \cdot 10^{-\frac{l_{EPL}}{10}} + T_{mr} \cdot \left(1 - 10^{-\frac{l_{EPL}}{10}}\right) \quad (\text{K}) \quad (11)$$

where l_{EPL} is the excess path loss attenuation and T_{mr} is the mean radiating temperature of the atmosphere. This formulation shows that when attenuation is low, the atmosphere contributes little additional noise and the observed temperature is close to the cosmic background value of 2.73 K. As attenuation increases, the atmosphere behaves more like a thermal source at its physical temperature, making atmospheric noise a dominant contributor at high frequencies and low elevation angles. This quantity represents the effective temperature of the absorbing and re-emitting atmospheric layer that contributes noise to the antenna. Rather than modeling each atmospheric layer individually, the ITU provides a simplified expression for the mean radiating temperature:

$$T_{mr}(f, P_s, T_s, \rho_{ws}) = \begin{cases} \alpha_t(f) + b_t(f) T_s \\ \quad + c_t(f) P_s \\ \quad + d_t(f) \rho_{ws}, & \text{No rain} \\ 275, & \text{Rain} \end{cases} \quad (\text{K}) \quad (12)$$

where T_s is the surface temperature in K, P_s is the surface pressure in hectopascals (hPa) and ρ_{ws} is the surface water vapor density in grams per cubic meter (g/m^3) [18]. The empirical coefficients $\alpha_t(f)$, $b_t(f)$, $c_t(f)$ and $d_t(f)$ are frequency-dependent parameters defined in ITU-R P.372-17 [18].

C. GROUND-STATION ANTENNA NOISE (DOWNLINK)

When calculating the ground station antenna noise temperature, most of the received noise power is collected through the main beam, which is directed toward the satellite, as shown in Fig. 6a. However, in practice the antenna also collects noise through sidelobes and spillover. For ground stations, these sidelobes couple to large portions of the atmosphere, which exhibit elevation-dependent brightness temperature due to variations in slant path attenuation, as discussed in Sec. IV-B. To account for this effect without requiring detailed antenna pattern data, the sidelobe contribution is approximated using a hemispheric average brightness temperature, $\bar{T}_{atm,hemi}$ [18]. This value is obtained by integrating the atmospheric brightness temperature (T_B) over the visible sky:

$$\bar{T}_{atm,hemi} = \frac{\int_0^{\pi/2} T_B(\theta) w(\theta) d\theta}{\int_0^{\pi/2} w(\theta) d\theta} \quad (\text{K}) \quad (13)$$

where the weighting function $w(\theta) = \cos(\theta)\sin(\theta)$ represents the projected solid-angle factor for an average antenna response when detailed sidelobe patterns are unavailable. This method incorporates the sidelobe spillover contribution into the effective antenna noise temperature, ensuring that the model accounts for both the main-beam atmospheric coupling and the background noise collected from wider angles. With $\bar{T}_{atm,hemi}$ determined, the effective antenna noise temperature for a ground station is expressed as:

$$T_{A,gs} = \eta_{gs} T_B + (1 - \eta_{gs}) \bar{T}_{atm,hemi} \quad (\text{K}) \quad (14)$$

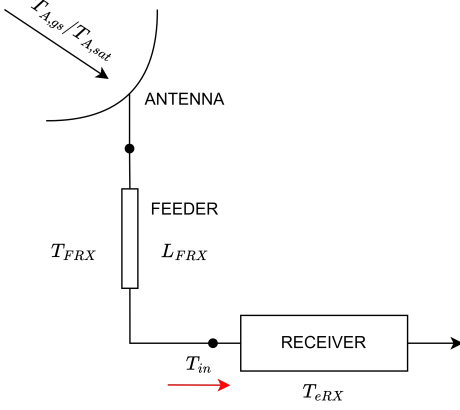


Fig. 7: Antenna noise contributions from the propagation channel (uplink or downlink) combined at the antenna input and attenuated by the feeder which connects the antenna with the receiver

with η_{gs} being the main-beam efficiency of the ground antenna and T_B is the brightness temperature calculated with Eq. 11 [19].

D. SATELLITE ANTENNA NOISE (UPLINK)

For the satellite, the antenna main beam is directed toward the Earth. In this case, the effective brightness temperature depends on both the surface emission and the reflection of downwelling atmospheric noise, as shown in Fig. 6b. The upwelling brightness temperature observed by the satellite is expressed as

$$T_{B,\text{sat}} = e_{\text{eff}} T_{\text{surf}} + (1 - e_{\text{eff}}) T_B \quad (\text{K}) \quad (15)$$

where e_{eff} is the effective surface emissivity, T_{surf} is the surface physical temperature and T_B is the atmospheric brightness temperature along the slant path [18]. Since the Earth is not a perfect blackbody radiator, part of the incident radiation is reflected or transmitted rather than fully absorbed. In contrast, space is effectively a cold background at ≈ 2.73 K, absorbing all incoming radiation and emitting only the cosmic microwave background. As a result, the Earth's surface has an emissivity less than unity $e_{\text{eff}} < 1$, which depends on factors such as soil type, vegetation cover, ocean surface conditions, frequency, and polarization. At Q/V band, the effective emissivity is adjusted for rain rate and constrained within a physically realistic range of $0.85 \leq e_{\text{eff}} \leq 0.995$. The surface temperature is taken from the interpolated meteorological data derived in Sec. II and corrected for diurnal heating, with a $+2$ K offset applied during daytime due to solar heating and no offset applied at night. The effective satellite antenna noise temperature is then given by

$$T_{A,\text{sat}} = \eta_{\text{sat}} T_{B,\text{sat}} + (1 - \eta_{\text{sat}}) T_{\text{cmb}} \quad (\text{K}) \quad (16)$$

where η_{sat} is the main-beam efficiency of the satellite antenna and $T_{\text{cmb}} = 2.73$ K is the cosmic microwave background temperature [19]. In this case, the spillover contribution is

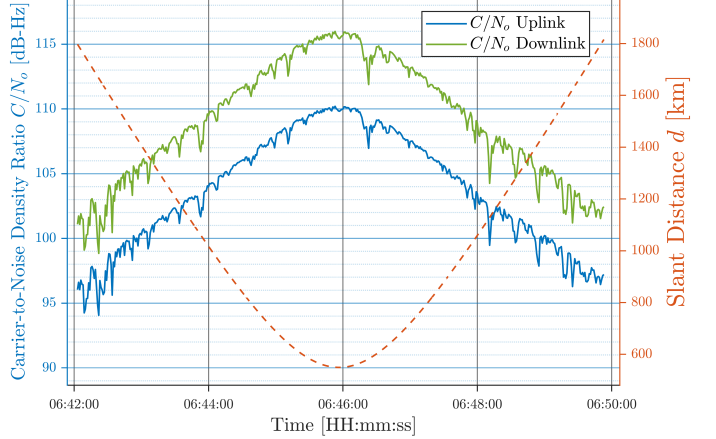


Fig. 8: Carrier-to-noise density ratio C/N_o for the uplink and downlink during the first pass of satellite 5, plotted alongside the corresponding slant distance d .

primarily from cold space rather than atmospheric emission, which contrasts with the ground station antenna. Finally, the total atmospheric thermal noise at the front end of the RF chain can be derived for both the uplink and downlink using Eq. 14 and Eq. 16, respectively. This quantity can be written as

$$T_{\text{in}} = \frac{T_A}{L_{\text{FRX}}} + \frac{(L_{\text{FRX}} - 1)T_{\text{FRX}}}{L_{\text{FRX}}} \quad (\text{K}) \quad (17)$$

where, L_{FRX} is the feeder loss, expressed as a linear factor and modeled as a passive element and T_{FRX} is the physical temperature of the feeder in K, as shown in Fig. 7 [2], [3]. Substituting this expression together with Eq. 10 into Eq. 8 provides the total system noise temperature T_{sys} .

E. CARRIER-TO-NOISE DENSITY RATIO (C/NO)

With the system noise temperature determined for both the uplink and downlink, the carrier-to-noise density ratio can be calculated. This parameter quantifies the strength of the received carrier relative to the noise power spectral density. By combining Eq. 1 with Eq. 7, the carrier-to-noise density ratio is obtained as

$$\left[\frac{C}{N_o} \right]_{\text{dB-Hz}} = \text{EIRP} + G_{\text{RX}} - L - 10 \log_{10}(k) - 10 \log_{10}(T_{\text{sys}}) \quad (18)$$

where $\text{EIRP} = P_{\text{TX}} - L_{\text{TX}} + G_{\text{TX}}$ is the effective isotropic radiated power in dB, G_{RX} is the receiver gain in dB, k is Boltzmann's constant and L is the total radio channel loss in dB [3]. The receiver feeder loss (L_{RX}) is treated as ideal in this analysis and is included in G_{RX} . Fig. 8 shows C/N_o for both the uplink and downlink. As expected, C/N_o peaks when the satellite passes near zenith, where the slant distance is shortest. The downlink consistently achieves a higher C/N_o . This difference is primarily due to antenna and receiver characteristics of both the satellite and ground station. Although the downlink experiences a higher system noise temperature, evident in the sharp dips of the green trace

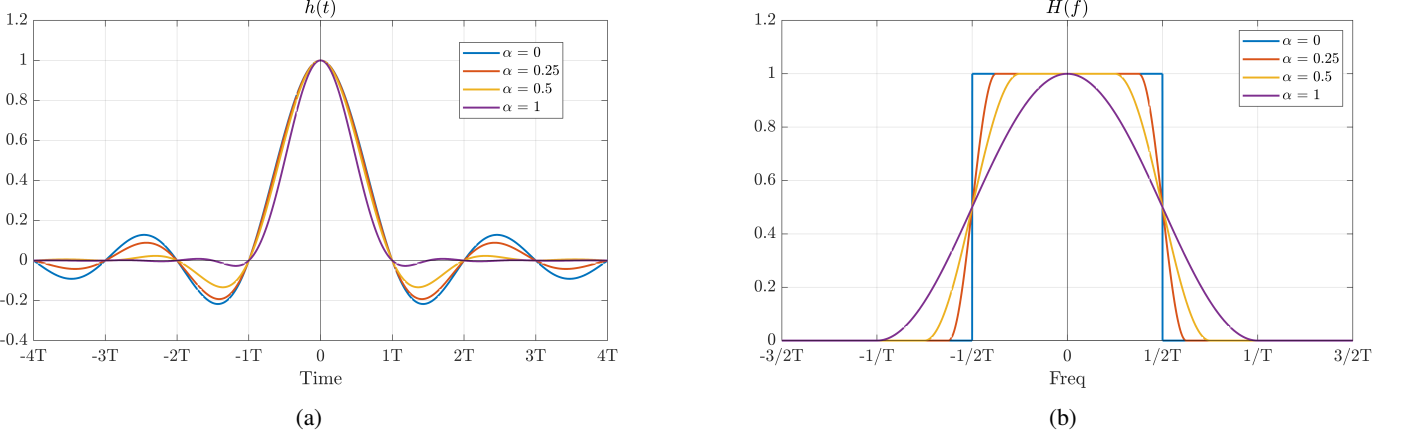


Fig. 9: Raised cosine filter response for different roll-off factors α with $\alpha = 0$ corresponds to the ideal Nyquist response. **(a)** Time-domain impulse response $h(t)$. **(b)** Frequency-domain response $H(f)$, showing the trade-off between bandwidth efficiency and side-lobe suppression.

caused by atmospheric emission coupled through sidelobes, consistent with Eq. 14. In contrast, the uplink receiver on the satellite has spillover that mainly views cold space, so its noise temperature is lower.

V. ADAPTIVE CODING AND MODULATION (ACM)

When transmitting a signal, modulation and coding are applied to achieve the desired data rate and ensure efficient use of the available spectrum. As illustrated in Fig. 8, C/N_0 varies over time, which makes the use of a fixed modulation and coding scheme inefficient and potentially unreliable, since the selected scheme may not match the instantaneous channel conditions. To overcome this limitation, adaptive coding and modulation (ACM) is employed. ACM is a link adaptation technique that dynamically adjusts both the modulation order and coding rate according to real-time channel quality [20]. Under favorable conditions, such as a high C/N_0 , the system applies higher-order modulation and higher coding rates to maximize throughput. In contrast, when channel conditions degrade and C/N_0 decreases, the system switches to more robust modulation and coding schemes to maintain link reliability. By continuously monitoring channel variations and selecting the most appropriate modulation and coding combination, ACM sustains the target data rate, improves spectral efficiency and reduces outage probability compared to static transmission schemes.

A. PULSE SHAPING AND ISI CONTROL

While ACM determines the most suitable modulation and coding scheme for the prevailing channel conditions, the transmitted signal must also be shaped to efficiently occupy the allocated spectrum and to be reliably detected at the receiver. This process, known as pulse shaping, shapes the waveform of each transmitted symbol prior to transmission. Without shaping, raw rectangular pulses produce sinc-shaped spectra with infinite bandwidth and strong sidelobes, which lead to poor bandwidth efficiency and potential violations of spectral mask

requirements. Rectangular pulses also introduce significant inter-symbol interference (ISI), since their long temporal tails overlap with adjacent symbols and distort symbol detection. Pulse shaping filters, such as the raised cosine (RC) and root-raised cosine (RRC), mitigate these issues by confining most of the signal energy within the allocated bandwidth while satisfying the Nyquist criterion for zero ISI [20]. The roll-off factor α of these filters controls the trade-off between occupied bandwidth and implementation complexity. A smaller roll-off factor improves spectral efficiency but requires sharper filtering, whereas a larger roll-off factor relaxes filter design at the expense of additional bandwidth, as illustrated in Fig. 9. The occupied bandwidth and corresponding system performance metrics are expressed by the following relationships. The symbol rate R_s is determined by the channel bandwidth B and the roll-off factor α [20]:

$$R_s = \frac{B}{1 + \alpha} \quad (\text{symbols/s}) \quad (19)$$

The bit rate R_b depends on the modulation order $k = \log_2(M)$ and the coding rate R_c :

$$R_b = R_s k R_c \quad (\text{bps}) \quad (20)$$

Here, R_c represents the redundancy introduced by forward error correction (FEC). The system spectral efficiency η_{sys} of an M-ary constellation is then given by [20]:

$$\eta_{\text{sys}} = \frac{k R_c}{1 + \alpha} \quad (\text{bps/Hz}) \quad (21)$$

These relationships demonstrate the interplay between bandwidth, roll-off factor, modulation order and coding rate. Pulse shaping directly influences spectral efficiency by controlling excess bandwidth, while ACM selects the optimal (M, R_c) pair to maximize throughput under varying channel conditions. Together, they ensure efficient spectrum utilization and robust performance in satellite communication systems.

B. SHANNON'S CAPACITY AND EB/NO THRESHOLDS

For this study, the ACM implementation is based on Shannon's channel capacity. Channel capacity defines the maximum theoretical data rate that can be transmitted over a communication channel with arbitrarily low error probability, given the channel bandwidth B and the energy-per-bit to noise density ratio E_b/N_o [21]. The parameter E_b/N_o represents the ratio of the energy allocated to a single information bit to the noise spectral density. It is related to the carrier-to-noise density ratio (C/N_o) and the bit rate R_b by

$$\frac{E_b}{N_o} = \frac{C}{N_o} - 10\log_{10}(R_b) \quad (\text{dB}) \quad (22)$$

With (C/N_o) expressed in dB-Hz [3]. As shown in Eq. 21 the modulation order M and coding rate R_c define the spectral efficiency of the selected modulation–coding pair. By applying Shannon's capacity expression [21], the achievable spectral efficiency η_c can be written as

$$\eta_c = \log_2 \left(1 + \eta_{\text{sys}} \cdot \frac{E_b}{N_o} \right) \quad (\text{bits/s/Hz}) \quad (23)$$

Rearranging for E_b/N_o yields

$$\left[\frac{E_b}{N_o} \right]_{\min} = \frac{2^{\eta_c} - 1}{\eta_c}$$

and in logarithmic form, including a practical implementation margin this becomes

$$\left[\frac{E_b}{N_o} \right]_{\min} = 10\log_{10} \left(\frac{2^{\eta_c} - 1}{\eta_c} \right) + \Delta_{\text{impl}} \quad (\text{dB}) \quad (24)$$

Here Δ_{impl} accounts for non-idealities such as coding inefficiencies, hardware limitations, and synchronization errors. This expression defines the theoretical lower bound on the E_b/N_o required to achieve reliable communication at spectral efficiency η_c , for each modulation order M and coding rate R_c , as calculated in Eq. 21.

C. MODCOD SELECTION WITH HYSTERESIS CONTROL

Building on these results, we now introduce the algorithm that governs the implementation of ACM. For each candidate MODCOD pair (M, R_c) , the following quantities are precomputed: (i) the symbol rate (R_c) from Eq. 19, (ii) the information bit rate R_b from Eq. 20 together with the system spectral efficiency η_{sys} from Eq. 21 and (iii) the required E_b/N_o threshold from Eq. 24. To resolve cases where two candidates provide nearly identical throughput, a tie-breaker is applied in the form of a slightly reduced reference bit rate

$$R_{b,\text{pref}} = R_b - \epsilon k \quad (\epsilon < 10^{-6})$$

which marginally favors the lower-order constellation. A deterministic fallback is also defined as the most robust candidate, corresponding to the minimum R_b , with ties resolved by selecting the smaller constellation k . These precomputed values constitute the static requirement table that the algorithm

uses during MODCOD selection. At run time, the selector processes the time series of C/N_o measurements (dB-Hz) for each pass. At every time index t , these values are converted into instantaneous E_b/N_o on an information-bit basis using Eq. 22. All candidates that satisfy

$$E_b/N_{o,\text{inst}} \geq E_b/N_{o,\text{req}}$$

form the feasible set. Within this set, candidates that exceed their thresholds by an additional upgrade margin H_{up} and provide higher throughput than the current mode are classified as upgrade-eligible. During initialization, the selector chooses the feasible candidate with the highest throughput, determined by $R_{b,\text{pref}}$. If no feasible candidate exists, the fallback option is used. To prevent rapid mode switching, a hysteresis policy is applied as outlined in the algorithm box. The decoder margin for the active MODCOD is defined as

$$\delta = E_b/N_{o,\text{inst}} - E_b/N_{o,\text{req}} \quad \text{If } \delta < H_{\text{down}}$$

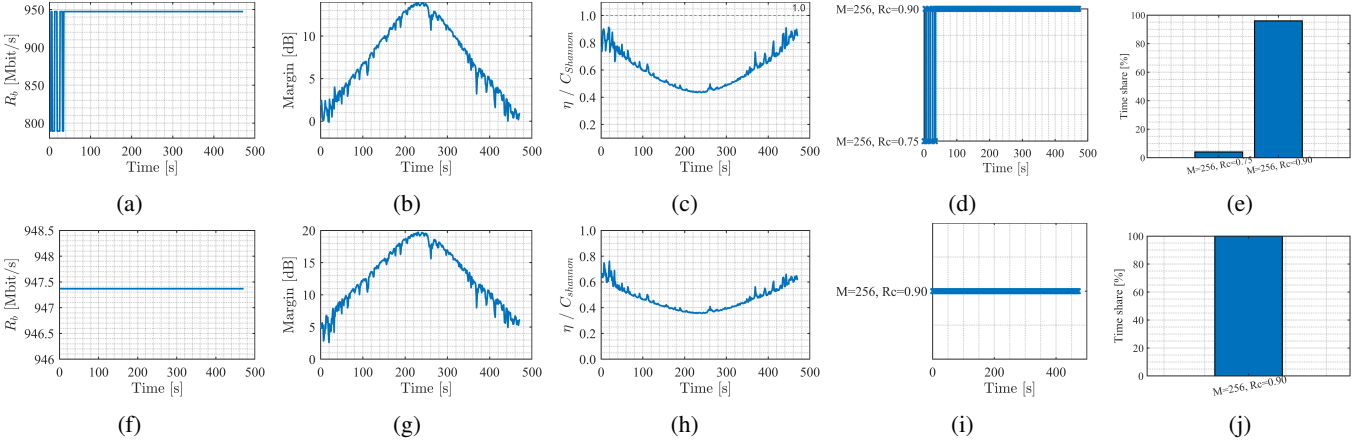
the selector immediately downgrades to the most robust feasible candidate. If no candidate is feasible, it reverts to the fallback. Otherwise, after a minimum dwell time t_{dwell} (measured in samples, equivalent to seconds only if the C/N_o sampling rate is 1 Hz), the selector upgrades only if a higher-throughput candidate is upgrade-eligible. If no such candidate exists, it retains the current mode. Missing or invalid C/N_o measurements trigger the fallback for the affected sample and reset the dwell timer to prevent spurious immediate upgrades. At each time index, the method records the selected $M(t)$, $R_c(t)$ and $R_b(t)$, along with the margin and a Boolean flag indicating whether fallback was applied. These outputs enable reproducible evaluation and parameter tuning. In our reporting, we include the exact (M, R_c) grid, the roll-off factor α , the occupied bandwidth B the sampling rate and any smoothing applied to the C/N_o sequence, as well as the values of Δ_{impl} , H_{up} , H_{down} and t_{dwell} . When measured per-MODCOD thresholds at the target BER or FER are available, they can be substituted for the Shannon-based thresholds without altering the algorithmic flow [20]. The full algorithm is available in the following GitHub repository [22].

VI. RESULTS

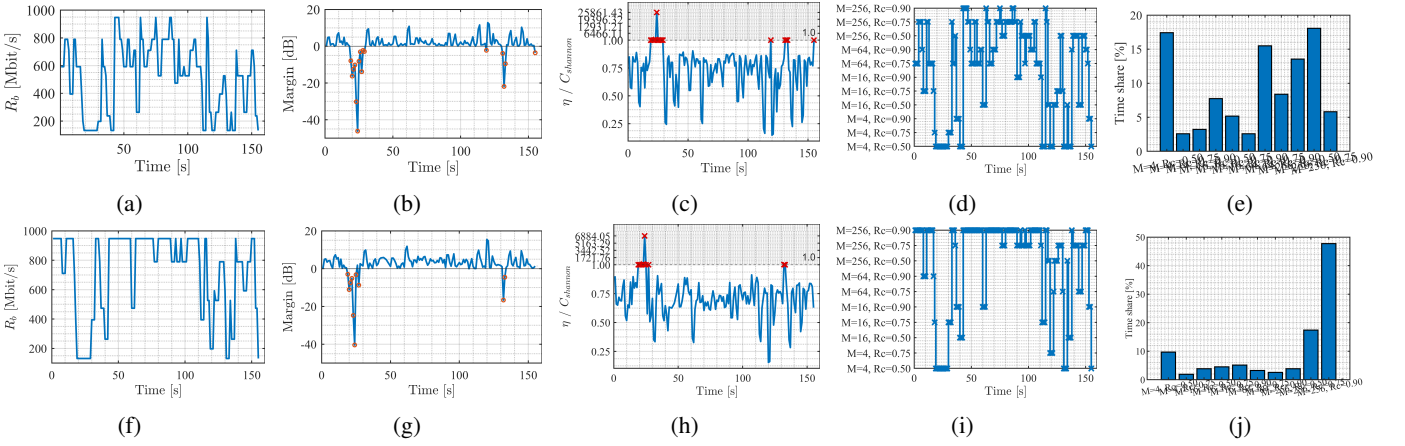
To demonstrate the behavior of adaptive coding and modulation (ACM) under different channel conditions, two satellite passes are analyzed. The first pass represents near-optimal conditions for both uplink and downlink, while the second represents the worst-case scenario for both links. The values in Appendix A are used to model the front-end noise and the gains of the receiver's internal electronics, while the values in Appendix B define the uplink, downlink and ACM parameters. Based on these inputs, the following results are obtained.

A. CASE STUDY I: STABLE LINK CONDITIONS

The first pass of satellite 5, occurring between 06:42:03 and 06:49:53 with a total duration of 7 minutes and 50 seconds, presents highly favorable conditions in which both the uplink



Satellite 5, pass 1: Subfigures (a)–(e) show the downlink and subfigures (f)–(j) show the uplink.



Satellite 2, pass 2: Subfigures (a)–(e) show the downlink and subfigures (f)–(j) show the uplink.

Fig. 10: Adaptive coding and modulation (ACM) results for two satellite passes. In the first pass of satellite 5, the downlink shows dynamic variations in data rate, margin and MODCOD, while the uplink remains more stable with an almost constant data rate and MODCOD. In contrast, the second pass of satellite 2 exhibits stronger variability. The downlink shows significant fluctuations in data rate, margin, efficiency and MODCOD selection, as reflected in the time allocation histogram, while the uplink also adapts dynamically but with fewer MODCOD transitions and a more concentrated time allocation.

and downlink operate at maximum efficiency, as shown in Fig. 10.

- 1) **Uplink:** In the uplink, the data rate remains essentially constant at approximately 947 Mbit/s throughout the entire duration of the pass, without any observable throughput drops. The link margin follows the expected geometric trend, starting at a few decibels, gradually increasing to values close to 18–20 dB near mid-pass, and then decreasing again as the satellite moves away. At no point does the margin approach 0 dB, indicating that ample headroom is maintained throughout the pass. The mode timeline confirms continuous operation at the highest available modulation and coding scheme, namely $M = 256$ with $R_c = 0.9$, with only brief fallback to 0.75 at the very beginning. This is reflected in the mode occupancy histogram, which shows nearly 100% usage of the highest-rate mode. The efficiency relative to the Shannon capacity follows a smooth trajectory, with values between 0.4 and 0.7. The efficiency decreases

slightly in the middle of the pass, when the channel capacity peaks, and recovers towards the end. This behavior reflects the fact that the selected MODCOD remains fixed while the theoretical capacity varies over time.

- 2) **Downlink:** The downlink exhibits nearly identical behavior. The data rate is again flat at around 947 Mbit/s with no interruptions, and the link margin steadily increases to nearly 20 dB before tapering off later in the pass. Although minor ripple variations are visible, these remain well above 0 dB and never compromise the link. The mode timeline shows uninterrupted operation in $M = 256$ with $R_c = 0.9$, and the occupancy histogram confirms exclusive use of this mode. The efficiency relative to Shannon also displays the characteristic U-shaped curve, with values ranging from 0.4 to 0.7, driven by changes in the channel capacity rather than switching events.

B. CASE STUDY II: DEGRADED LINK CONDITIONS

The second pass of satellite 2, occurring between 08:06:00 and 08:08:34 with a total duration of 2 minutes and 34 seconds, experiences severe fading caused by low elevation angles and radio channel losses. As a result, ACM must adapt continuously to preserve connectivity, as shown in Fig. 10.

- 1) **Uplink:** In the uplink, the data rate is highly unstable, fluctuating between 900 Mbit/s and values as low as 200–300 Mbit/s, with repeated collapses throughout the pass. These drops correspond to deep fades in the link margin, which exhibits strong variability and several excursions below -40 dB. Such events drive the ACM controller to switch aggressively between modes. The mode timeline reveals rapid transitions across the entire range of MODCODs, from high-efficiency $M = 256$ at $R_c = 0.9$ down to $M = 4$ at low coding rates during the deepest fades. The system spends little time in any one mode, reflecting the highly dynamic channel. The occupancy histogram confirms this by showing time shared among nearly all available modes, with significant usage of mid- and low-order modulation schemes. The efficiency relative to Shannon fluctuates accordingly, typically between 0.5 and 0.8, with brief overshoots above unity during the most severe fades, which are artifacts of the margin calculation under unstable conditions.
- 2) **Downlink:** The downlink shows similar degraded behavior. The data rate is characterized by frequent interruptions, with extended intervals below 500 Mbit/s and several drops close to outage levels. The margin is unstable, with values oscillating in the 0–10 dB range and several deep fades falling well below 0 dB. These events force the ACM algorithm to switch constantly, as illustrated by the mode timeline, which shows repeated cycling through nearly all MODCODs. The occupancy histogram confirms this, with time distributed broadly across the modulation and coding set rather than concentrated in a single mode. The efficiency relative to Shannon is again highly variable, remaining mostly between 0.4 and 0.8, with sharp disturbances corresponding to the deepest fades.

VII. DISCUSSION

In Sec. III, real-time measurements would be preferable to the 10-minute interval data that must be interpolated to 1-second resolution, as interpolation introduces a margin of error, although small in this case. In Sec. II and Sec. IV, accurate modeling of both the ground station and satellite antennas is essential for reliable noise temperature estimation. In addition, detailed modeling of the electronic components is required to improve the accuracy of the noise temperature calculation and provide a closer approximation of the channel. In Sec. V, further in-depth study is needed. Specifically, appropriate bandwidth allocation must be defined, and additional work is required on channel coding, pulse shaping, and related aspects, since placeholder values were used in this study that do not fully represent practical conditions. Further investigation

is also required to determine which modulation scheme is most suitable, as this work only identifies the best MODCOD pair without addressing the broader choice of modulation. The use of OFDM should also be considered, as it can improve performance and mitigate inter-symbol interference. Finally, established communication protocols must be adopted to ensure compliance with regulatory requirements [12].

VIII. CONCLUSION

This study introduced a comprehensive framework for modeling the link budget of LEO Q-band satellite communication systems and for selecting the appropriate modulation and coding rate based on the link performance. The framework incorporates both internal thermal noise, originating from electronic components, and atmospheric thermal noise encountered during signal propagation in the uplink and downlink. These factors were integrated into an adaptive coding and modulation (ACM) algorithm based on Shannon's capacity theorem, enabling the dynamic selection of modulation and coding schemes according to real-time channel conditions throughout a satellite pass. Beyond performance evaluation, the framework provides a basis for practical applications such as satellite constellation management, where it can assist in eliminating unsuitable candidates and identifying the optimal satellite for handover. Future work may extend this approach by incorporating measured hardware parameters, advanced channel models, and standardized communication protocols to further align the framework with operational scenarios.

APPENDIX A RECEIVER FRONT-END NOISE AND GAINS

Since the internal electronics of the ground station and satellite receivers have not been modeled, assumed values representative of Q-band operation are used.

TABLE I: Front end noise and gain summaries by node.

| Node | Noise temperatures [K] | Gains [dB] | Attenuator |
|------|------------------------|-----------------------|--------------------------|
| GS | $T_{\text{LNA}} = 120$ | $G_{\text{LNA}} = 20$ | $T_{\text{ATT}} = 300$ K |
| | $T_{\text{MX}} = 2450$ | $G_{\text{MX}} = -3$ | $L_{\text{ATT}} = 2$ dB |
| | $T_{\text{IF}} = 170$ | | |
| SAT | $T_{\text{LNA}} = 290$ | $G_{\text{LNA}} = 30$ | $T_{\text{ATT}} = 300$ K |
| | $T_{\text{MX}} = 4000$ | $G_{\text{MX}} = 5$ | $L_{\text{ATT}} = 2$ dB |
| | $T_{\text{IF}} = 290$ | | |

APPENDIX B LINK BUDGET AND ACM PARAMETERS

In practice, the bandwidth B is allocated by the ITU and the national telecommunications agencies of each country [12], [13]. For this study, we assume the allocation of a wideband channel for both uplink and downlink. Since the satellite and ground station antennas have not been modeled, we further assume good antenna efficiency. The gains and transmit powers are treated as estimates, as no detailed component modeling has been performed to provide values representative of real deployments. The modulation rates are selected as multiples of four, consistent with quadrature amplitude modulation (QAM) schemes.

TABLE II: Directional link and ACM parameters, uplink and downlink, with EIRP.

| Parameter | Uplink | Downlink | Unit |
|-----------------|------------------|------------------|--------|
| f_c | 43 | 42 | GHz |
| B | 250 | 250 | MHz |
| α | 0.9 | 0.9 | — |
| η_{GS} | 0.90 | 0.90 | — |
| η_{SAT} | 0.88 | 0.88 | — |
| P_{TX} | 29 (14.6 dBW) | 41 (16.1 dBW) | W, dBW |
| L_{TX} | 2 | 2 | dB |
| G_{TX} | 41 | 55 | dBi |
| EIRP | 53.6 | 69.1 | dBW |
| G_{RX} | 38 (satellite) | 25 (ground) | dBi |
| L_{RX} | 2 | 2 | dB |
| M | {4, 16, 64, 256} | {4, 16, 64, 256} | — |
| R_c | {1/2, 3/4, 9/10} | {1/2, 3/4, 9/10} | — |
| Δ_{impl} | 1.2 | 1.2 | dB |
| H_{up} | 0.5 | 0.5 | dB |
| H_{down} | 0.2 | 0.2 | dB |
| t_{dwell} | 3 | 3 | s |

Note: seconds for t_{dwell} apply when the C/N_0 sampling rate is 1 Hz.

APPENDIX C KEPLERIAN ELEMENTS AND ORBIT SETUP

TABLE III: Keplerian Orbital Elements Used to Simulate the LEO Satellite Trajectories

| Name | a [km] | e [°] | i [°] | Ω [°] | ω [°] | v [°] |
|-------|--------|-------|-------|--------------|--------------|-------|
| SAT-1 | 550 | 0 | 52 | 23 | 12 | 45 |
| SAT-2 | 550 | 0 | 67 | 151 | 178 | 289 |
| SAT-3 | 550 | 0 | 83 | 87 | 245 | 133 |
| SAT-4 | 550 | 0 | 74 | 201 | 33 | 72 |
| SAT-5 | 550 | 0 | 96 | 314 | 99 | 210 |

Here, a denotes the semi-major axis, e the orbital eccentricity, i the inclination, Ω the right ascension of the ascending node (RAAN), ω the argument of perigee and v the true anomaly.

REFERENCES

- [1] G. Maral, M. Bousquet, and Z. Sun, *Satellite Communications Systems: Systems, Techniques and Technology*. Hoboken, NJ Chichester, West Sussex: Wiley, sixth edition ed., 2020.
- [2] L. J. Ippolito, *Satellite Communications Systems Engineering: Atmospheric Effects, Satellite Link Design and System Performance*. New York Academy of Sciences Series, Newark: John Wiley & Sons, Incorporated, 1st ed ed., 2017.
- [3] NASA Jet Propulsion Laboratory, *DSN Telecommunications Link Design Handbook (810-005)*, 2014. [Online], Accessed: Aug. 28, 2025.
- [4] International Telecommunication Union, “Attenuation by Atmospheric Gases and Related Effects,” ITU-R P.676-13, 2022.
- [5] International Telecommunication Union, “Specific Attenuation Model for Rain for Use in Prediction Methods,” ITU-R P.838-3, 2005.
- [6] International Telecommunication Union, “Attenuation due to clouds and fog,” ITU-R P.840-9, 2023.
- [7] International Telecommunication Union, “Characteristics of precipitation for propagation modeling,” ITU-R P.837-7, 2017.
- [8] IPCC, *Climate Change 2021: The Physical Science Basis*, 2021. [Online], Accessed: Aug. 28, 2025.
- [9] I. Ziargas and A. Kourtras, “Simulation Framework for Q/V-Band Excess Path Loss Forecasting in LEO Satellite Links Using Deep Learning.” ResearchGate, Sept. 2025.
- [10] National Observatory of Athens, “Patra (Prosfygika) Weather Station.” <https://penteli.meteo.gr/stations/patra-prosfygika/>. [Online]. Accessed: Aug. 28, 2025.

- [11] National Observatory of Athens. <https://www.noa.gr/en/>. [Online]. Accessed: Aug. 28, 2025.
- [12] Internationale Fernmelde-Union, ed., *Final Acts: World Radiocommunication Conference, WRC-19*. Geneva: International Telecommunication Union, 2020.
- [13] Hellenic Telecommunications & Post Commission. <https://www.eett.gr/en/>. [Online], Accessed: Aug. 28, 2025.
- [14] Hellenic Telecommunications & Post Commission, “National Regulation on the Allocation of Radio Frequency Bands.” <https://www.eett.gr/en/operators/radio-frequency-spectrum/radiospectrum-licensing/satellite-service/>. [Online]. Accessed: Aug. 28, 2025.
- [15] O. A. Alduchov and R. E. Eskridge, “Improved Magnus Form Approximation of Saturation Vapor Pressure,” Apr. 1996.
- [16] World Meteorological Organization, *Guide to Instruments and Methods of Observation (WMO-No. 8)*, 2018.
- [17] J. Shaw, “Radiometry and the Friis transmission equation,” *American Journal of Physics*, vol. 81, pp. 33–37, Jan. 2013.
- [18] International Telecommunication Union, “Radio noise,” ITU-R P.372-17, 2024.
- [19] “IEEE Standard for Definitions of Terms for Antennas,” IEEE Std 145-2013 (Revision of IEEE Std 145-1993), pp. 1–50, Mar. 2014.
- [20] European Telecommunications Standards Institute, “Implementation Guidelines for DVB-S2,” DVB TR 102 376-1, 2014. [Online], Accessed: Aug. 28, 2025.
- [21] C. E. Shannon, “A mathematical theory of communication,” *The Bell System Technical Journal*, vol. 27, no. 3, pp. 379–423, 1948.
- [22] I. Ziargas and P. Zervas, “Link Budget Modeling for Q/V-Band LEO Satellite Communications with Adaptive Coding and Modulation.” GitHub Repository. [Online], Accessed: Aug. 28, 2025.